https://doi.org/10.5194/wes-2025-286
Preprint. Discussion started: 22 January 2026

Impact of Boundary Layer Height and Large-Scale Turbulence on the Efficiency and Loads of Offshore Wind Farms

Stefan Ivanell[1], Bjarke T. Olsen[2], Antoine Mathieu[3,4], Cristina Mulet-Benzo[5,6], Abdul Haseeb Syed[2], Warit Chanprasert[1], Mikael Sjöholm[2], Jakob Mann[2], and Julia Gottschall[5,6]

[1]Uppsala University, Department of Earth Sciences, Division of Wind Energy, Visby, Sweden
[2]Technical University of Denmark, Dept. of Wind and Energy Systems, Roskilde, Denmark
[3]EDF R&D, 6 Quai Watier,78400 Chatou,France
[4]CEREA, École des Ponts, Île-de-France
[5]Fraunhofer Institute for Wind Energy Systems IWES, Bremen, Germany
[6]University of Bremen, Faculty of Geosciences, Bremen, Germany

Correspondence: Stefan Ivanell (stefan.ivanell@geo.uu.se)

Abstract.

The increasing scales of modern wind energy systems, with rotor diameters exceeding 250m and hub heights above 150m, introduces new challenges in understanding interactions between atmospheric dynamics and wind farm performance. This study investigates the impact of atmospheric boundary layer height (BLH) as a key parameter influencing wind farm efficiency and turbine loads. Using mesoscale simulations from the Weather Research and Forecasting (WRF) model combined with lidar measurements, we quantify BLH variability and its associated uncertainty across three representative sites in the North and Baltic Seas. A series of Computational Fluid Dynamics (CFD) simulations for a wind farm, containing 100 15MW turbines, under varying BLH and wind speed conditions reveal significant efficiency differences linked to atmospheric stratification, with lower BLH generally reducing farm efficiency. Seasonal and site-specific climatologies highlight that Baltic Sea conditions, characterized by larger extent of low BLH conditions, lead to reduced performance compared to North Sea sites. Furthermore, we assess the influence of large-scale coherent turbulence structures on turbine loads through aeroelastic simulations of both bottom-fixed and floating configurations. The results show that low-frequency fluctuations, often absent in standard design models, increase fatigue loads within wind farms, particularly for turbines in wake-affected regions. These findings underscore the need to incorporate BLH variability and large-scale turbulence effects into engineering models for reliable performance and load predictions of next-generation offshore wind farms.

1 Introduction

The scale of modern wind energy systems is rapidly increasing. Turbines with rotor diameters exceeding 250m and hub heights above 150m are now being deployed, particularly in offshore environments. This shift toward larger rotors, larger wind farms, and more closely spaced installations introduces a range of new scientific challenges. As turbine dimensions expand, the interaction between atmospheric boundary layer (ABL) dynamics and rotor-scale flow becomes increasingly complex (Veers et al., 2019). Turbines now operate across a wider vertical span of the atmosphere, often traversing multiple layers of stratification or turbulence regimes. These vertical variations in wind speed and direction significantly affect turbine loading, wake behavior, and ultimately energy production. In parallel, the growth in wind farm size introduces mesoscale flow effects and long-range wake interactions, including farm-to-farm interference, that challenge traditional siting and modelling approaches. Understanding how atmospheric conditions interact with wind farms at these larger scales is critical for accurate prediction of energy yield, structural loads, and long-term performance. This includes questions such as: How does the boundary layer height impact the wind farm efficiency? How does the estimated wind farm efficiency vary with boundary layer height model/measurement uncertainty? To what extent will the boundary layer height annual variation impact loads and farm efficiency considering different physical locations. Can one conclude a link between these phenomena and the wind farm efficiency and loads if comparing e.g. a position in the North Sea to a position in the Baltic Sea, where it is known that the atmospheric conditions vary considerably, resulting in e.g. a larger extent of low level jets in the Baltic Sea?

Atmospheric features such as stability, turbulence intensity, and low-level jets, along with phenomena emerging from the use of larger rotors and larger wind farms, such as flow blockage, modified vertical entrainment, and complex wind farm wake dynamics, are all intricately connected. These interactions span a range of spatial and temporal scales and are highly sensitive to the state of the atmospheric boundary layer. In this study, we used the boundary layer height (BLH) as a central parameter to characterize the state of the atmosphere. A shallow boundary layer is typically associated with stable stratification and increased occurrence of low-level jets, whereas deeper boundary layers are indicative of convective conditions and stronger buoyancy-driven turbulence. Since vertical mixing and entrainment processes are strongly governed by the boundary layer structure, the BLH serves as a physically meaningful proxy for the atmospheric mixing potential. Importantly, as modern wind turbines increasingly operate at or even above the boundary layer height, their interaction with the capping inversion and the overlying free atmosphere becomes non-negligible. This can suppress or alter vertical entrainment, modify wake recovery, and influence overall farm efficiency. Using the BLH as a representative metric, our aim is to capture the collective influence of stratification, turbulence, and flow confinement on wind farm performance in a conceptually unified and computationally practical manner.

As the BLH is a central component for atmospheric variations and wind farm impact, it proves important to understand the uncertainty of model to measurement. The BLH can be defined in various ways depending on stability conditions, thus inducing uncertainty in the model output. Hu et al. (2010) compared radiosonde data to three WRF boundary layer schemes, finding sensitivities particular to each scheme depending on vertical mixing strength and resulting entrainment and stability parameters. Guo et al. (2024) conducted another sensitivity analysis of radiosonde data to a reanalysis dataset. They found various dependencies ranging from heat flux, land properties, and near-surface meteorological conditions. Xi et al. (2024) compared offshore BLH radiosonde from a ship campaign to ERA5 outputs, demonstrating that the model tends to "smooth" the BLH, overestimating at low heights and underestimating at greater heights. Olson et al. (2019) focuses more on the ABL scheme MYNN, finding that stable conditions are not well represented. This is due to tuning features in the scheme, where the heat flux in stable conditions may be higher than necessary to prioritize surface temperature accuracy, thus inducing a potential overestimation of the BLH. These studies support the uncertainty modeled BLH could provide, thus leading to misrepresented wind farm efficiencies. To understand this BLH impact, this study includes a comparative analysis of the modeled BLH and lidar-measured BLH to quantify this uncertainty.

This work was carried out within the FLOW (Atmospheric Flow, Load and pOwer for Wind energy) project funded by the EU Horizon Europe programme (grant no. 101084205). The goal of the FLOW project is to develop novel engineering tools for modern GW-scale wind farms' power and load predictions, as well as to provide open source datasets of both experiments and high-fidelity simulations for the wind industry. In a previous study within FLOW, Ivanell et al. (2025) compared how different models can reproduce farm efficiency and its dependence on the boundary layer height. This study uses the same approach but with a wider parameter space to map different atmospheric conditions and then assess their impact by connecting these cases with the climatology at three selected sites.

This paper is structured according to the following. In section 2 Methodology, we give a motivation to the selected methodology and describe the selected points of interest for the study. We also describe the data available from different measurement data sets. Here we also describe the numerical methods used. In further detail, we describe the methodologies used for uncertainty assessment and load assessment. In section 3 Results, we present the results of wind resource mapping and farm efficiency simulations. The results of the uncertainty and load assessments are here also presented. In section 4 Discussion, we discuss the results. In section 5 Conclusions, we present our final conclusions of this study.

2 Methodology

2.1 Motivation

The selection of the simulation approach is a compromise between accuracy and reasonable numerical cost to map the parameter space needed. By using a similar approach as in (Ivanell et al., 2025), we ensure that the medium-fidelity Reynolds Averaged Navier Stokes (RANS) code used here well represents the cases addressed since good agreement with high-fidelity codes in similar settings was shown in that previous work.

The simulation cases representing different atmospheric conditions are then connected to the climatology of three selected sites. These sites are picked because of their variation, but also because of the knowledge of corresponding flow features provided within the FLOW project. The climatology is created by WRF simulations and is further described in section 3.1.

2.2 Description of sites

Figure 1 illustrates the locations of the three selected sites used in this study. We use uppercase letters for modeled sites for investigations and lowercase letters for measurement data points. Site A is located at Dogger Bank, an area of great interest for large offshore wind installations. Site B and b are located at the Danish west coast and corresponds to the site Trans, one larger field campaign within the FLOW project. Site C is located in the Baltic Sea, where wind conditions are known to differ significantly from those of the North Sea. (Hallgren et al., 2023) Site d corresponds to Høvsøre, site e to measurements from FINO1, and location f corresponds to measurements from the Hywind Scotland site.

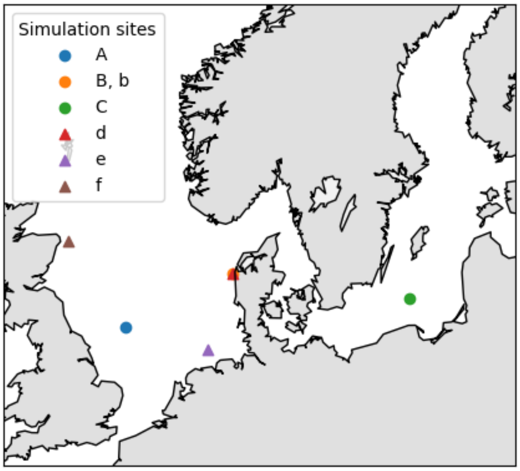

Figure 1. The figure illustrates the selected sites A, B and C in Northern Europe used in the FLOW project and here used for this case study. A is located at Dogger Bank, B at Trans at the Danish west coast, and C is a location in the Baltic Sea. b, d, e, and f represent points from where measurements have been used for uncertainty calibration. Site b corresponds to measurements carried out at location B, site d corresponds to Høvsøre, site e corresponds to FINO1, and site f is a location at Hywind Scotland.

2.3 Numerical setup

Numerical simulations are conducted using the open-source CFD code $code\_saturne$ (Archambeau et al., 2004). The simulation is carried out for a 100 15MW wind turbine wind farm in a staggered configuration under conventionally neutral conditions. The numerical setup is the same as in (Ivanell et al., 2025), where further details can be found. Additional configurations are modeled in order to cover a wider range of the parameter space in terms of boundary layer heights (BLH) and geostrophic wind speeds. Simulations with geostrophic wind speeds of 5, 8, 10, 12 and $15\ \mathrm{ms}^{-1}$ are run for boundary layer heights of 150, 300, 500 and $1000\ \mathrm{m}$ resulting in a total of 20 simulations.

The climatological basis of this study is a mesoscale hindcast simulation made using the Weather Research and Forecasting (WRF) model (ARW; version 4.2.1) (Olsen et al., 2025). The dataset spans a five-year period from summer 2019 to 2024 and consists of a model domain covering the North and Baltic Sea areas, with a horizontal grid spacing of three kilometers and 85 vertical levels, including 15 levels in the lowest 300 meters of the atmosphere. The model's initial and boundary conditions come from ERA5 pressure-level data, MM5 similarity (Jiménez et al., 2012) as the surface layer scheme, and (Zhang et al., 2018) (3DTKE) was used as the PBL scheme.

2.4 Available experimental data

Measurements from site b are used to quantify the uncertainties associated with the BLH data used within the study, and are further described in 2.4.1. The primary objective of analyzing measurements from sites d, e, and f is to quantify the scale of large-scale coherent structures in the marine atmosphere, which may impact the fatigue loads and power production of large offshore wind turbines. To that extent, the spectral measurements from these sites were fitted with an atmospheric turbulence model specifically designed for large-scale horizontal structures (Syed and Mann, 2024a). The large-scale structures are quasi-two-dimensional; hence, this type of model is referred to as the *2D turbulence model* hereafter. The one-hour spectral measurements are fitted to the 2D turbulence model along with a three-dimensional turbulence model, as described in Mann (1994) and Mann (1998). Both 2D and 3D atmospheric turbulence models include a scaling parameter (c and $\alpha\epsilon^{2/3}$), a length scale parameter (L_{2D} and L_{3D}), and an anisotropy parameter (ψ and Γ).

2.4.1 Measurements from Trans (b)

A measurement campaign for studying the lateral coherence of the turbulent flow in an offshore environment was conducted during the spring of 2024 within the FLOW project. The campaign site is located on the west coast of Denmark adjacent to the Høvsøre wind turbine test center (d) with relatively low terrain behind the shore which provides offshore conditions undisturbed by topography without the need to be far away from the shore. The campaign used five scanning lidars in staring mode on the shore in order to simultaneously measure the wind in six cross-points over the sea about 1 km from the shore where two lidars were placed at a northern site close to the lighthouse in Bovbjerg and three lidars were located next to the church in Trans.

This site also hosted a scanning lidar that was configured to perform vertical stare measurements to obtain the BLH measurements. A WCS200 alternated from a 5-minute Doppler beam swinging scan for horizontal wind speed retrievals, and a 2-minute fixed vertical scan; only the vertical scan was used for the BLH derivation. Table 1 contains further lidar configuration information. The BLH was determined from a blackbox tool specific for the WCS. Further information on the lidar BLH derivation algorithm and the measurement campaign are found in (Mulet-Benzo et al., 2025) and (Mann et al., 2026), respectively.

Table 1. FLOW scanning strategy for the scanning lidar

Scan Name	Scan Type	Duration [s]	Elevation [°]	Accumulation Time [ms]	Pulse length [m]	Min Range [m]	Max Range [m]	Display Range [m]
VAD	PPI	480	45	1000	25	100	3075	25
ABL	Fixed	120	90	1000	25	50	3025	25

2.4.2 Measurements from Høvsøre (d)

The wind turbine test center at Høvsøre is located on the west coast of Denmark. The test center also features a state-of-the-art meteorological mast that measures atmospheric parameters at heights ranging from 2 to 116.5 m. The mast experiences unobstructed wind from the west and south directions. Here, we utilize the turbulence measurements recorded by the mast at four heights above ground, i.e., 40 m, 60 m, 80 m and 100 m. The measurements were recorded at a frequency of 20 Hz. The 2D turbulence spectra model is fitted to the measured spectra, and the model parameters are evaluated under different atmospheric stability conditions.

The scaling parameter of the 2D turbulence in Høvsøre exhibits patterns similar to those observed at FINO1, as depicted in Figure 2. The observed magnitudes across various atmospheric conditions and at different altitudes align closely with those noted at FINO1. However, the 2D turbulence anisotropy parameter ψ presents a different picture. At wind speeds below 15 ms^{-1} and for frequencies below 10^{-3} Hz, the lateral (S_v) and horizontal (S_u) spectral components are nearly identical in all categories of atmospheric stability, indicating slight anisotropy in 2D turbulence at Høvsøre. Under neutral atmospheric conditions, turbulence exhibits anisotropy at wind speeds exceeding 15 ms^{-1}; the patterns for stable and unstable conditions remain indeterminate due to the limited available data.

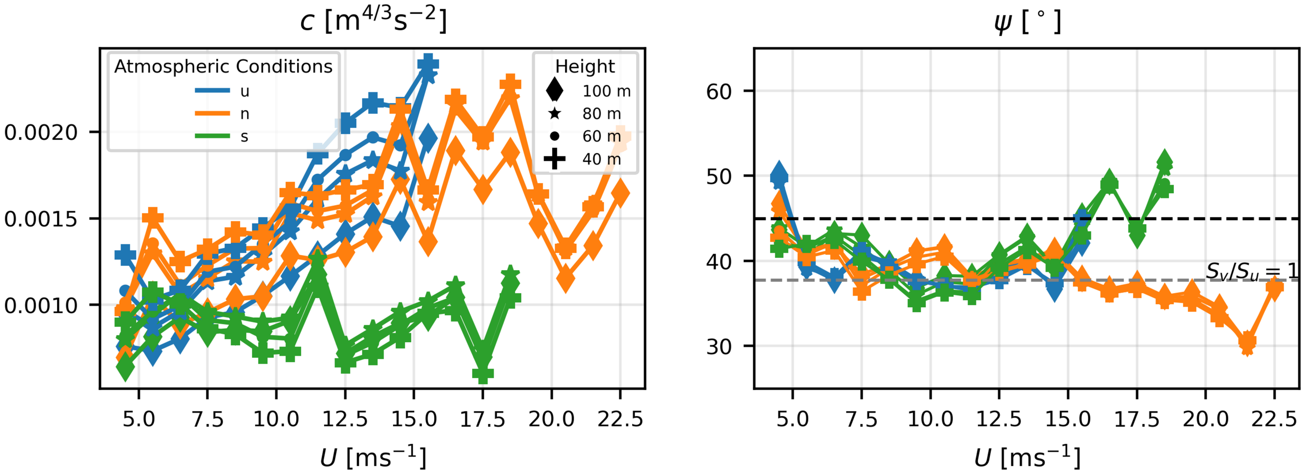

Figure 2. 2D turbulence model parameters obtained through the least-square fitting of the observed turbulence spectra at Høvsøre. The three colors represent different atmospheric stability conditions. The markers denote four different measurement heights. The grey dashed line represents the ψ value at which S_v/S_u = 1. ψ = 45° (the black dashed line) represents isotropic 2D turbulence

2.4.3 Measurements from FINO1 (e)

The FINO1 research platform is located in the German Bight in the North Sea, approximately 45 km north of the island of Borkum. The platform features multiple instruments that measure meteorological, hydrographic and sea-state parameters. The platform was deployed to provide offshore resource assessment for wind power projects in the North Sea. Since 2009, numerous offshore wind farms have been commissioned in the vicinity, and the measurements at FINO1 are significantly influenced by the wake flows from neighboring wind farms. For the analysis presented in this article, we selected the 2 years of data before the commissioning of the surrounding wind farms, i.e., from January 2007 to December 2008. During that period, three Gill R3-50 sonic anemometers were mounted at 41.5 m, 61.5 m and 81.5 m above mean sea level. These sonic anemometers recorded the three wind velocity components (u, v, w) and the air temperature (T) at a sampling frequency of 10 Hz. One-hour wind component spectra were obtained from the three sonic anemometers for wind speeds ranging from 4 to 23 ms^{-1}. Figure 3 and

4 illustrate the variation of 2D and 3D turbulence spectra scaling and anisotropy parameters, respectively, under three different stability conditions, i.e., unstable (u), neutral (n), and stable (s). The model parameters shown here are obtained at 81 m above mean sea level; however, the results at other heights (not shown here) revealed a minimal impact of altitude. The 2D turbulence at the FINO1 test site can be considered as isotropic turbulence, since the ψ value stays around 45° for all wind speed values. Figure 4(b) shows that the 3D turbulence anisotropy values (Γ) have an increasing trend with the mean observed wind speed.

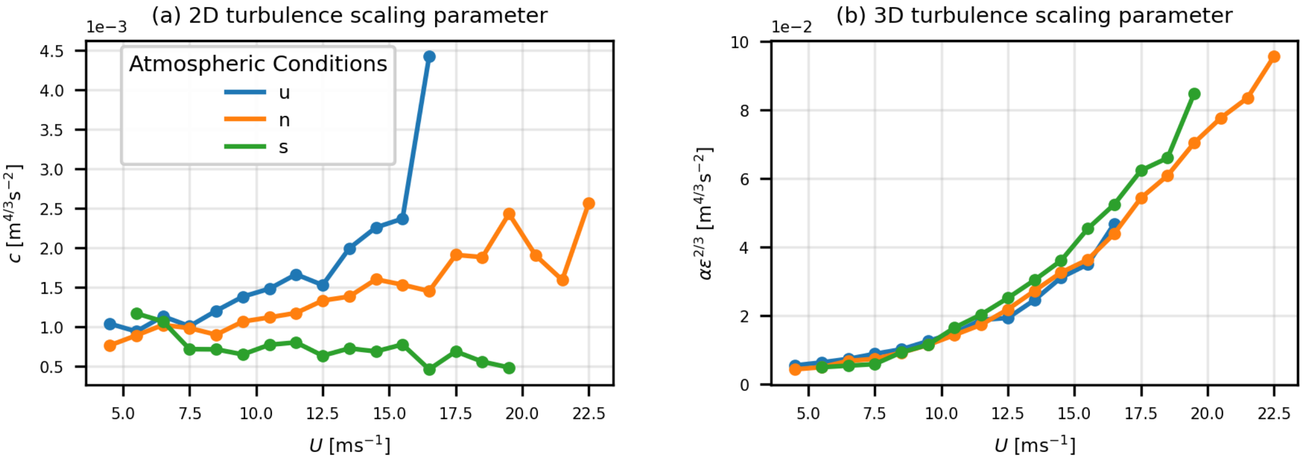

Figure 3. Turbulence spectra scaling parameters obtained from fitting the one-hour measured spectra at the FINO1 test site for (a) 2D turbulence model, and (b) 3D turbulence model under three different stability conditions, i.e., unstable (u), neutral (n), and stable (s).

2.4.4 Measurements from Hywind Scotland (f)

29 km east of the coast of Scotland, the world's first commercial floating offshore wind farm, *Hywind Scotland*, was commissioned in 2017. The wind farm contains five 6 MW floating wind turbines with a hub height of 98.4 m and a rotor diameter of 154 m. On two of these wind turbines, a WindIris pulsed wind lidar measured line-of-sight (LOS) velocities from four beams oriented at different azimuth and tilt angles. The lidars measured LOS velocities at 10 different range gates, spanning 50 to 400 m, for eight months in 2019 and 2020. A detailed description of lidar measurements and data processing is provided in (Angelou et al., 2023) and (Syed and Mann, 2024a). LOS velocity spectra were obtained for selected 1-hr time periods and were fitted with the 2D and 3D turbulence models. The model-fitting results showed that the large-scale turbulence at this location is highly anisotropic, as ψ was mostly found in the range of 20°-30°. It was also observed that large-scale fluctuations dominated the turbulence spectra under stable conditions, while the 3D turbulence held more energy under neutral conditions.

2.5 Uncertainty assessment methodology

The uncertainty of the climatologies referred to in this study is assessed by the measurements provided at site b, see figure 1, where this location overlaps with the modeled site B, therefore allowing a direct comparison between measurements and mod-

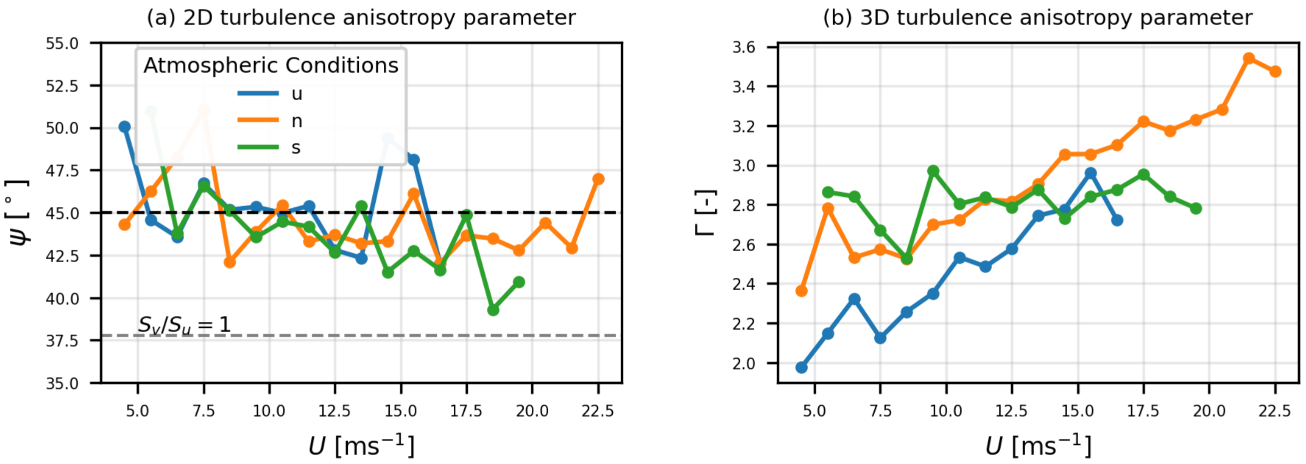

Figure 4. Turbulence spectra anisotropy parameters obtained from fitting the one-hour measured spectra at the FINO1 test site for (a) 2D turbulence model, and (b) 3D turbulence model under three different stability conditions, i.e., unstable (u), neutral (n), and stable (s). A value of 45° represents isotropic 2D turbulence. The dashed grey line in (a) represents the ψ value where the low-frequency u and v components' spectra are of equal magnitude.

eling of the BLH. This will therefore be used to assess the uncertainty of the BLH based on WRF simulations. Measurements from d, e and f are used to assess the horizontal large turbulence scales, i.e., the low-frequency part of the wind turbulence spectrum, to assess its impact on loads.

2.6 Load assessment methodology

Marine atmospheric turbulence is often dominated by large-scale, horizontally coherent structures, which represent the low-frequency portion of the wind turbulence spectrum. Such large scales span tens of kilometers and have timescales exceeding 600 seconds, the standard timescale for wind turbine load simulations. Here, we investigate the impact of the large-scale horizontal turbulence on wind turbine loads and wake development inside a wind farm. Synthetic wind fields containing low-frequency fluctuations, i.e., 2D turbulence, down to 1 hr^{-1} are used in aeroelastic simulations with the DTU HAWC2 aeroelastic code. The IEA 15 MW reference wind turbine (Gaertner et al., 2020) is used in both fixed and floating configurations to investigate the impact of low-frequency wind fluctuations on the loads and response of the wind turbine system. Synthetic wind fields containing both small-scale and large-scale turbulence were generated using the model and methodology outlined by Syed and Mann (2024a, b). To generate realistic offshore wind fields, the model parameters for generating synthetic wind fields were derived from two years of undisturbed wind flow observations at the FINO1 test site in the North Sea, shown in Fig. 3 and 4. To holistically compare the effect of large-scale turbulence structures on a wind turbine response and loads, three different types of turbulent wind fields were used as inputs. These include: (i) pure small-scale turbulence wind fields, referred to as 3D turbulence, (ii) mixed large-scale and small-scale turbulence, referred to as 2D+3D turbulence, and (iii) 3D turbulence wind fields scaled to match the turbulence intensity of 2D+3D turbulence wind fields.

The HAWC2 aero-elastic code, developed by the Technical University of Denmark (DTU), is used to perform load simulations based on a multibody formulation, where each body is modeled as a Timoshenko beam with both bending and torsional deflections. DTU Wind Energy controller (Meng et al., 2020) was used for pitch regulation and other control strategies in the three operating ranges of the wind turbine: (i) 3 $\mathrm{ms}^{-1} \leq \overline{U} \leq 6.98$ ms^{-1} where there is a constant rotor speed of 5 rpm and a proportional-integral (PI) controller regulates the torque, (ii) 6.98 $\mathrm{ms}^{-1} < \overline{U} \leq 10.59$ ms^{-1} where there is optimal tip speed ratio (TSR) and the blade pitch angles are zero, and (iii) 10.59 $\mathrm{ms}^{-1} < \overline{U} \leq 25$ ms^{-1} where the rotor speed is regulated via PI controller on the blade pitch angles such that the rotor does not exceed its rated speed of 7.55 rpm. In the floating configuration, an additional tower-top velocity feedback loop is implemented to prevent excessive pitch instability at wind speeds exceeding the rated value. A wave field based on the Pierson–Moskowitz spectrum with the same input parameters is used for all the simulations. A significant wave height, $H_s = 1.83$ m, and wave peak period, $T_p = 7.44$ s, are chosen. To reduce stochastic uncertainty from turbulent wind fields, 20 random seeds were used to generate wind fields for all 22 wind speed bins from 3 to 25 ms^{-1}. Turbulence boxes were created with the following specifications: the number of grid points in three directions is $N_x = 32,768,\ N_y = N_z = 128$, the grid spacing in the longitudinal direction was variable depending on the mean wind speed, and the grid spacing in the lateral and vertical directions was constant, i.e., $d_y = d_z = 4$ m. This allows us to have lateral and vertical dimensions of the boxes more than double the rotor diameter of the wind turbine, thereby avoiding the periodicity issues outlined in Mann (1998) and Syed and Mann (2024b).

3 Results

3.1 Wind statistics

To provide a climatology and BLH for site A, B, and C, WRF simulations have been carried out from which the BLH is extracted, see section 2.3.

Figure 5 illustrates the variation of BLH for a selected period and site. The wind speed and boundary layer height distribution on site A, B and C are illustrated in figure 6. Panels (d) and (e) further highlight the difference between C and A and B and A, respectively. The distributions show that that lower BLH occurring to a higher extent going from A to B and even slightly more going from A to C.

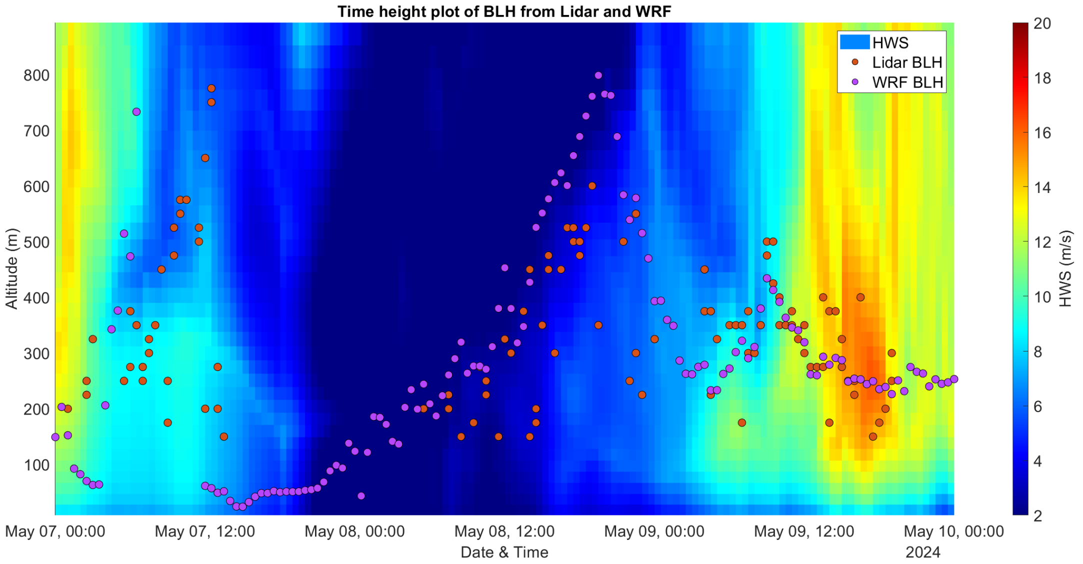

Figure 5. The figure illustrates mesoscale data for a selected period and the identification of the BLH from both the WRF and lidar retrievals, where HWS is the horizontal wind speed.

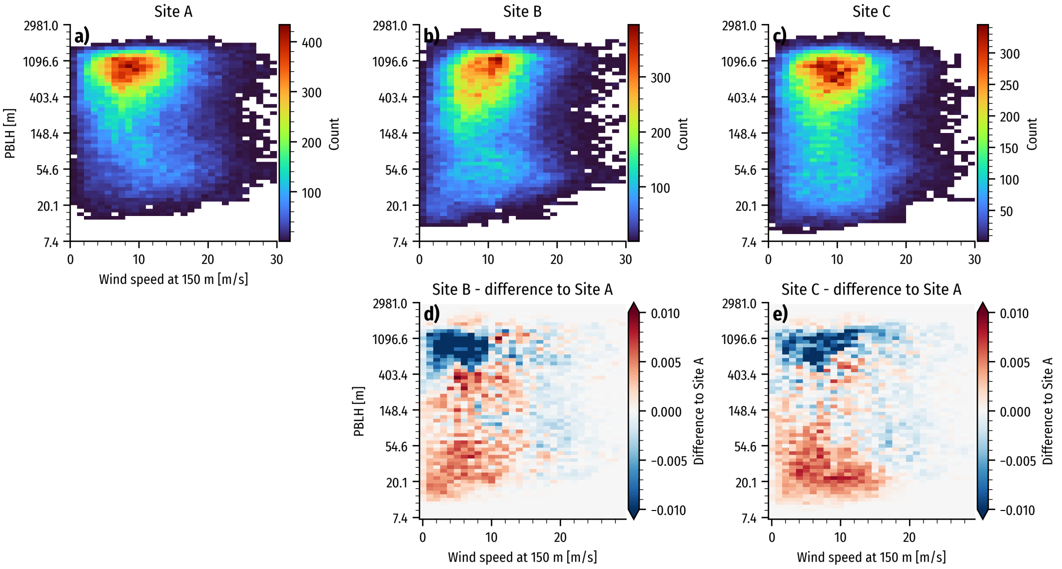

Figure 6. Occurrence counts of PBL height and hub-height wind speed combinations at sites A, B, and C. Panels (d) and (e) show the difference in the density between sites B and A, and C and A, respectively.

3.2 Results of farm efficiency simulations

The following section shows results from simulations of four BLHs for five wind speeds ranging from 5 to $15 m/s$. The power was calculated by $T \times U_d$ where T is thrust and U_d is the local average disc velocity. Non-local effects efficiency η_{nl} and local wake efficiency η_w are quantified by the following definitions as introduced by Allaerts and Meyers (2018).

$$\eta_w = \frac{P_{\text{tot}}}{N\,P_1}, \tag{1}$$

where P_{tot} describes the total wind farm power output, N number of turbines in a farm and P_1 is the power of front-row turbines. The losses due to non-local effects, i.e. the blockage effect can be expressed as:

$$\eta_{nl} = \frac{P_1}{P_\infty}, \tag{2}$$

where P_∞ is obtained from single turbine simulations. The total wind farm efficiency η_f is the product of the local and non local efficiencies.

3.2.1 Farm efficiency based on power calculated from $T \times U_d$

The results from the farm simulations show that the farm efficiency does depend on the BLH to a great extent. Figure 7 illustrates the non-local efficiency according to equation 2, the local efficiency according to equation 1, i.e., wake losses and the total farm efficiency as a function of BLH and wind speed. Tables 2 to 5 show numerical values of non-local, local, and total farm efficiencies. The largest variations in efficiency can be seen for subrated wind speeds for both non-local and local efficiency as expected. However, with a clear variation of the local efficiency for the most extreme BLH.

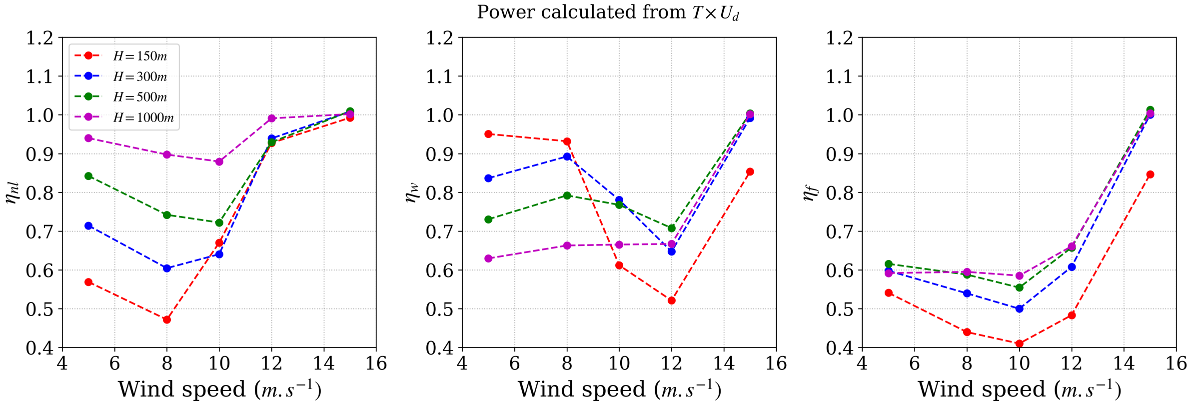

Figure 7. Non-local effects efficiency η_{nl}(left panel), wake efficiency η_w (middle panel) and wind farm efficiency η_f (right panel) as a function of wind speed and BLH. Efficiencies are calculated using the power as the thrust multiplied by the average rotor wind speed.

Table 2. Wind Farm Efficiencies for $H = 150m$ and power calculated from $T \times U_d$

WS $(m.s^{-1})$	η_{nl}	η_{w}	η_{f}
5	0.619	0.951	0.589
8	0.513	0.932	0.478
10	0.733	0.612	0.449
12	0.921	0.521	0.48
15	0.992	0.853	0.847

Table 3. Wind Farm Efficiencies for $H = 300m$ and power calculated from $T \times U_d$

WS $(m.s^{-1})$	η_{nl}	η_{w}	η_{f}
5	0.776	0.837	0.649
8	0.658	0.893	0.587
10	0.694	0.781	0.542
12	0.932	0.647	0.603
15	1.007	0.992	0.999

Table 4. Wind Farm Efficiencies for $H = 500m$ and power calculated from $T \times U_d$

WS $(m.s^{-1})$	η_{nl}	η_{w}	η_{f}
5	0.919	0.731	0.672
8	0.806	0.792	0.638
10	0.784	0.768	0.602
12	0.927	0.708	0.656
15	1.008	1.004	1.011

https://doi.org/10.5194/wes-2025-286
Preprint. Discussion started: 22 January 2026

Table 5. Wind Farm Efficiencies for $H = 1000m$ and power calculated from $T \times U_d$

WS $(m.s^{-1})$	η_{nl}	η_{w}	η_{f}
5	0.940	0.630	0.592
8	0.897	0.663	0.595
10	0.880	0.665	0.585
12	0.990	0.667	0.661
15	1.002	1.002	1.004

3.2.2 Farm efficiency mapped back to frequency distributions at sites

In this section, we present the result of the simulation results related to the specific climatology at sites A, B, and C, according to the methodology described in section 2.

The wind farm efficiency results presented above provide data points for specific hub-height wind speeds and boundary layer heights. Here, we combine those results with the underlying climatology of hub-height wind speeds and boundary layer heights obtained from the mesoscale dataset. In Fig. 8, the two-dimensional histogram of these two variables is shown at site C (subplot a), with the sparse wind farm efficiency datapoints indicated by black marks. In subplots b-g, the efficiency data are mapped via a linear-distance-weighted radial-basis function to the full span of the underlying weather data. The mapping function yields interpolation within the bounds of the efficiency data and extrapolation outside, with a strong dependence on the edge nodes.

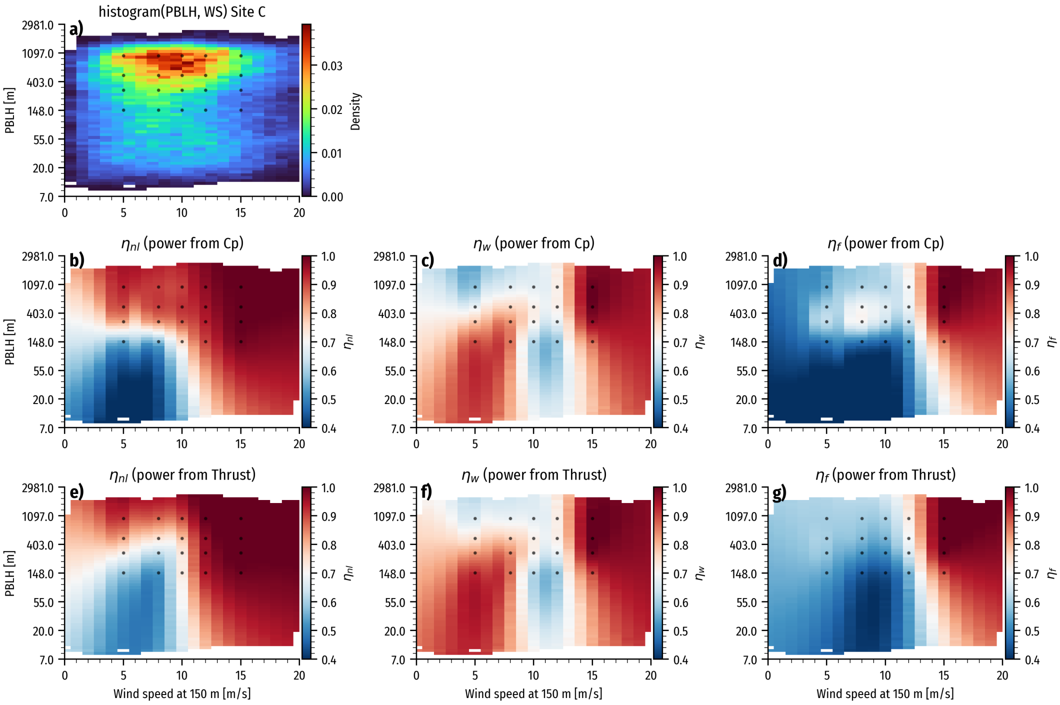

Figure 8. Wind farm efficiencies mapped onto the 2D probability of occurrence histogram bins. The black dots mark the actual underlying wind farm cases run with CFD. Efficiency values are mapped from the original points to the histogram bins using a linear RBF interpolator.

3.3 Impact on farm efficiency

This section presents the result of the climatological mean farm efficiency at sites A, B, and C, computed as a weighted-average efficiency using the underlying wind speed and boundary-layer height distribution as the weights (e.g., Fig. 8 subplot a) and the simulated efficiencies mapped to the distribution (Fig. 8 subplot b-g). This weighted average is estimated using both the Cp and Thrust methods, and is done for the full climatology (five years), as well as seasonal averages.

The results in figure 9 show how the local and non-local blockage in total varies between the sites A, B and C but also the seasonal variations. More details on seasonal variations of the climatology can be found in Appendices A1-A4. The local blockage, i.e., the result of wake interaction within the wind farm has a limited overall variation. However, seasonal variations can be seen. The non-local efficiency, i.e., the farm blockage do vary between the sites where sites with larger share of stable conditions do have lower efficiency. That trend is most obvious for the spring and summer periods, while it is not that clear for other seasons. The total efficiency also shows the same trend since this is the sum of both local and non-local efficiencies, where the variations are most influenced by the non-local efficiencies.

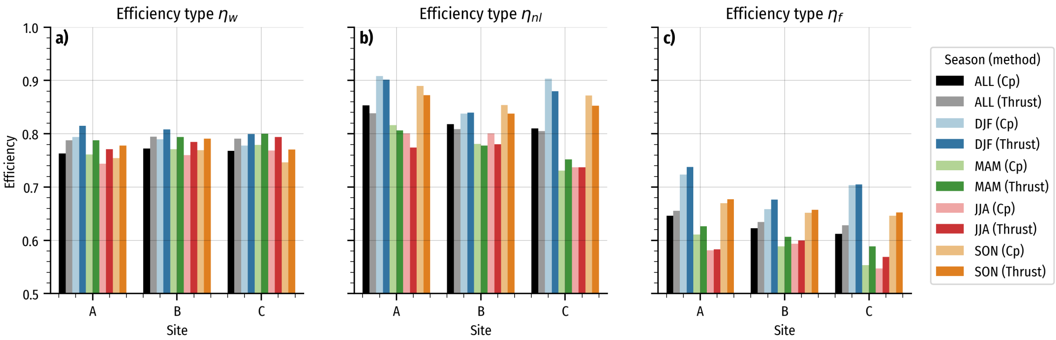

Figure 9. Average efficiencies for site A, B, and C, using the mapped efficiencies in Fig. 8.

Table 6. Total weighted-average efficiencies η_f for the three sites (Identical to values in Fig. 8, panel c.)

	Season	ALL	DJF	MAM	JJA	SON
Site	Method					
A	Cp	0.645848	0.723224	0.610803	0.581411	0.669561
	Thrust	0.655542	0.737395	0.626288	0.583289	0.676849
B	Cp	0.622901	0.658582	0.588785	0.593742	0.651428
	Thrust	0.634622	0.676520	0.606232	0.599480	0.657230
C	Cp	0.612231	0.703728	0.553627	0.547208	0.646325
	Thrust	0.628251	0.704938	0.588722	0.568630	0.652310

3.4 Uncertainty quantification

Using scanning lidar data measurements at the evaluation site B, we can assess the uncertainty of the BLH extracted from the WRF dataset. The following section describes that evaluation, and conducts an uncertainty assessment of the wind farm efficiencies based on the BLH uncertainty from the WRF dataset.

On site B, a scanning lidar was configured to conduct vertical scans to measure vertical wind speed and carrier-to-noise ratio (CNR) that were then used to derive the BLH. A combination of gradient method and image processing was applied to both the radial wind speed and CNR to obtain the mixing layer height, here interpreted as the BLH. Further information on the methodology is published by Mulet-Benzo et al. (2025). The measurement campaign lasted from February to June 2024, generating a total of 5 months of data.

Table 7 summarizes the key performance indicators (KPI's) of the WRF and lidar BLH bias. The bias was averaged for the overall dataset as well as per season; note that the dataset was limited to fulfill the winter and summer season. The BLH bias was averaged for each time period, yielding mostly underestimations from WRF compared to the lidar dataset. The root mean square error (RMSE) indicates a significant deviation of the WRF to lidar BLH, ranging between 340-380m. Figure 10 further shows the statistical distribution of the bias via whisker plots. Though the bias is quite low, the whisker plots show a wide spread of the quantiles, demonstrating the variability of the under and overestimation of WRF BLH compared to lidar retrievals for all seasons.

Table 7. Key performance indicators for the BLH analysis between WRF and lidar retrievals. A negative bias means an underestimation from WRF.

Time Period	Average of Bias	RMSE	Data Count
Overall	-32	376	2859
F	-73	344	402
MAM	-38	384	2186
J	-70	359	271

Figure 10. Whisker plots demonstrating the statistical distribution of the BLH bias from WRF and lidar. Each box represents a time period, "Overall" for all the data and the rest for seasonal categorization, i.e., MAM for data in spring, F and J for the remaining data (no full months) in February and June.

As there is a clear uncertainty in the BLH WRF retrievals, an evaluation was conducted to assess how this uncertainty could impact the wind farm efficiencies. Figure 11, similar to Figure 6, demonstrates the 2D efficiency values but strictly visualizes the data for the four BLH WRF scenarios per wind speed bin: 150m, 300m, 500m, and 1000m. The lidar and WRF combined dataset were binned in a similar way; Figure 12 demonstrates the data count spread of the 5 month dataset for each bin of BLH and wind speed. For each bin of BLH and wind speed, a quantile analysis was conducted to find the first and third quantiles of the BLH bias; this provides an indication of the bias variability, accounting for over and underestimations of the WRF BLH compared to the lidar. These quantile values were then applied to the bin center, here the four BLH WRF scenarios. Based on a linear interpolation from Table 2 to Table 5 to multiple BLH heights, a range of efficiencies could be obtained from the upper 270 and lower BLH values within each bin.

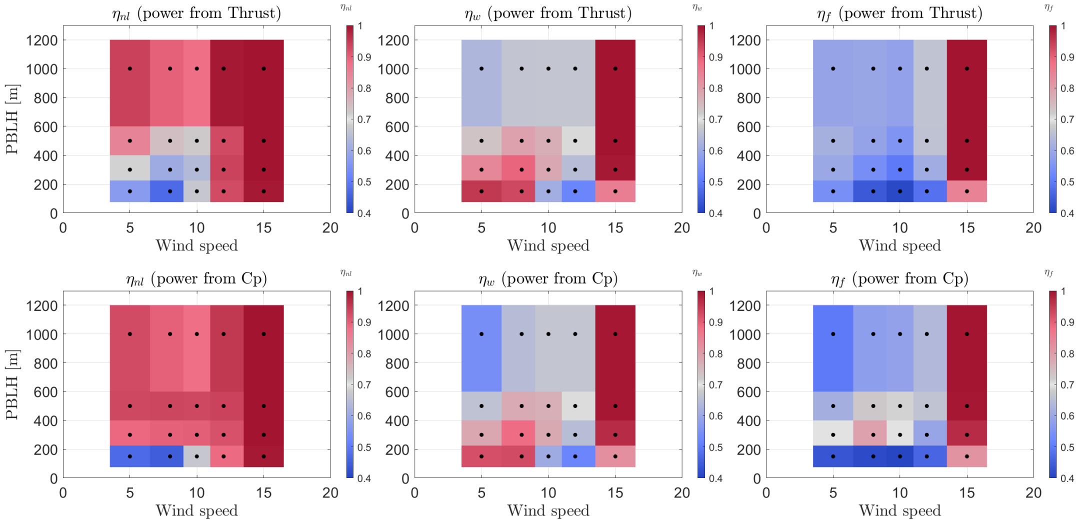

Figure 11. Similar to Figure 6, the wind farm efficiences are plotted strictly to the 4 BLH height scenarios the WRF dataset was run for.

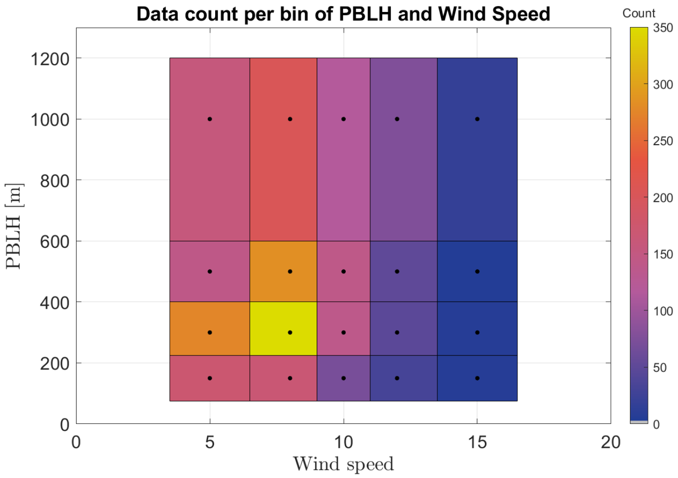

Figure 12. Similar to Figure 6, the wind farm efficiences are plotted strictly to the 4 BLH height scenarios the WRF dataset was run for.

Figure 13 demonstrates the flow logic for the quantile methodology to determine the efficiency uncertainty from the BLH bias per bin. The final results are shown in Figure 14 as 2D graphs similar to Figure 11. The figure demonstrates the range of efficiencies per bin, highlighting the variability of the wind farm efficiency due to the variability of the boundary layer height. The heatmap demonstrates that, for all types of efficiencies, the higher the wind speed and greater the BLH, the lower the 275 uncertainty of the efficiency. For lower wind speeds and boundary layer height below 500m, the efficiencies vary much more.

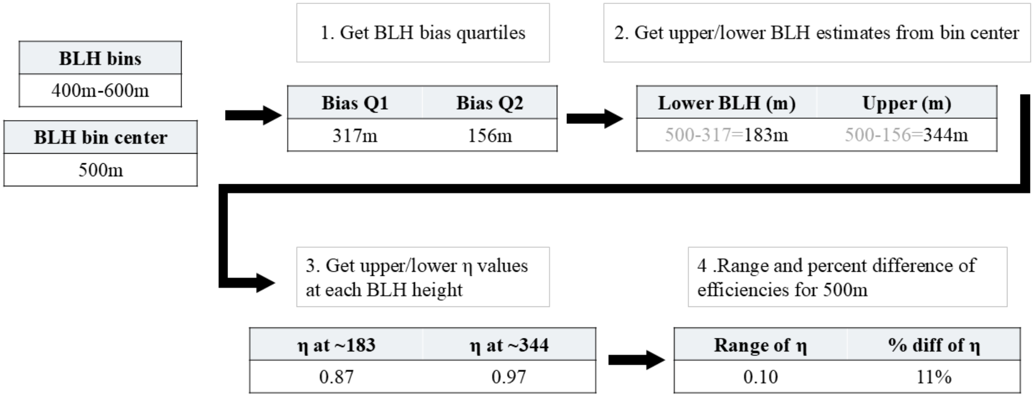

Figure 13. Flowchart providing an example for calculating efficiency uncertainty at BLH 500m.

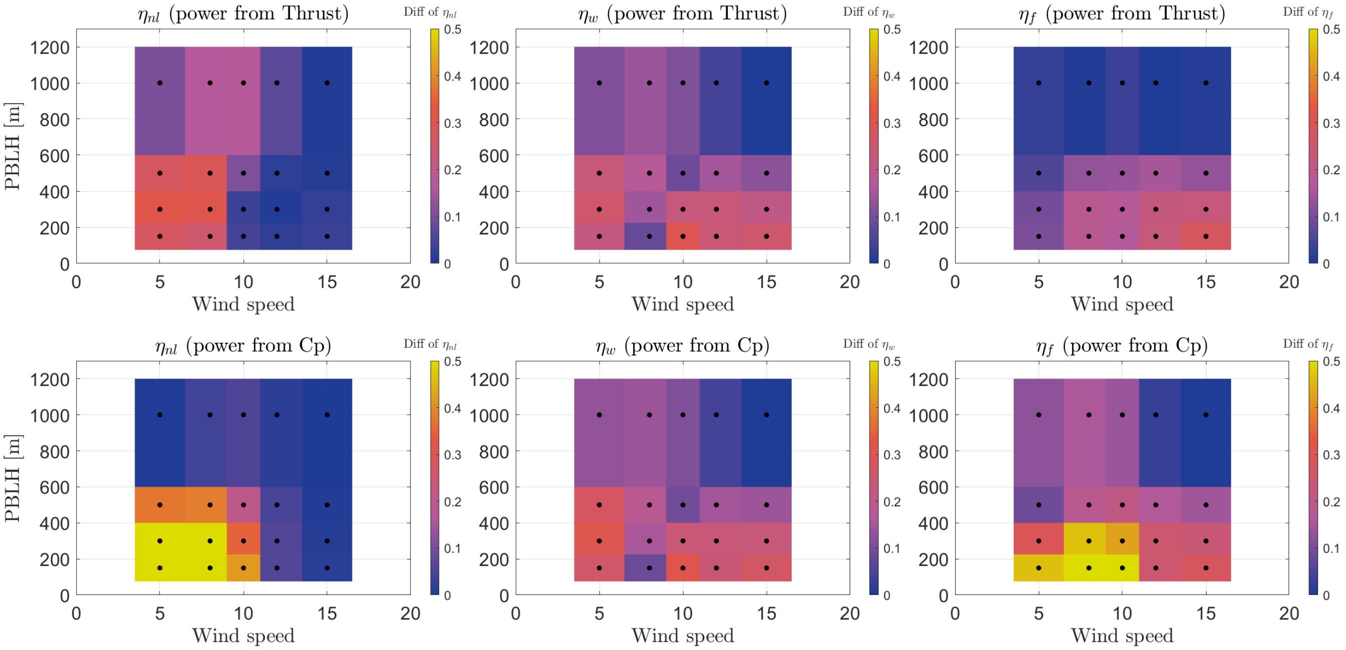

Figure 14. 2D plot demonstrating range of efficiencies per bin of wind speed and boundary layer height.

Table 8 provides the upper and lower ranges of efficiency for all wind speeds and all boundary layer heights, quantifying the range of efficiencies based on the BLH uncertainty.

	η_w		η_{nl}		η_f	
	Cp	Thrust	Cp	Thrust	Cp	Thrust
Upper	0.78	0.80	0.79	0.83	0.62	0.61
Average	0.77	0.79	0.78	0.78	0.58	0.60
Lower	0.74	0.76	0.62	0.68	0.54	0.50

Table 8. Uncertainty performance metrics for η_w, η_{nl}, and η_f

3.5 Large-scale coherent structures impact on wind turbine loads

To evaluate how the boundary layer height impacts the turbine loads we assess the correlation between BLH and horizontal large scale turbulence. By evaluating sites d, e, and f according to figure 1, we can evaluate how loads are related to turbulence scales and how this differs in different site characteristics, here examining the impact on sites A, B, and C.

3.5.1 Standalone wind turbine

Both fixed and floating configurations of the IEA 15 MW wind turbine showed an increased dynamic response to large-scale turbulence structures. Fig. 15 and 16 show the response of tower foreaft and blade loads in response to three different kinds of wind fields at three different wind speeds. These wind speeds represent three different operating regions of the wind turbine: below-rated speed, 4.5 ms^{-1}, rated wind speed, 10.5 ms^{-1}, and above-rated wind speed, 16.5 ms^{-1}. In the top row of both figures, the full frequency response is shown in terms of the Power Spectral Density (PSD) of the tower fore-aft moment. A peak corresponding to the monopile tower's first mode, i.e., 0.17 Hz, is visible at all three wind speeds in the tower's response, while the 1P, 2P, and 3P frequencies are distinctly visible in the blade's response. Both tower and blade moments show an increased response to the low-frequency wind turbulence, which can be visible below 2×10^{-3} Hz. Similarly, this response decreases with an increase in the wind speed. In the case of the floating configuration, an increased pitch and surge response in the floater motion was also observed from the low-frequency wind fluctuations. This led to higher mooring line tension loads as shown in Fig. 17.

3.5.2 Wind farm wake dynamics

To understand the effect of large-scale coherent structures on wind farm wake dynamics, flow simulations were conducted on a small wind farm containing 16 IEA 10-MW wind turbines. These wind turbines have a rotor diameter of 198 m and a hub height of 119 m. The turbines were arranged in a regular grid of four rows, with the second and fourth rows offset in the transverse direction. We utilize a wind farm aeroelastic framework called DYNAMIKS (Liew et al., 2023), which integrates a Dynamic Wake Meandering (DWM) model (Larsen et al., 2008) with a parallelized wind turbine aeroelastic code (HAWC2), enabling the generation of dynamic load data for each wind turbine within the farm. The DWM model utilizes turbulence boxes

https://doi.org/10.5194/wes-2025-286
Preprint. Discussion started: 22 January 2026

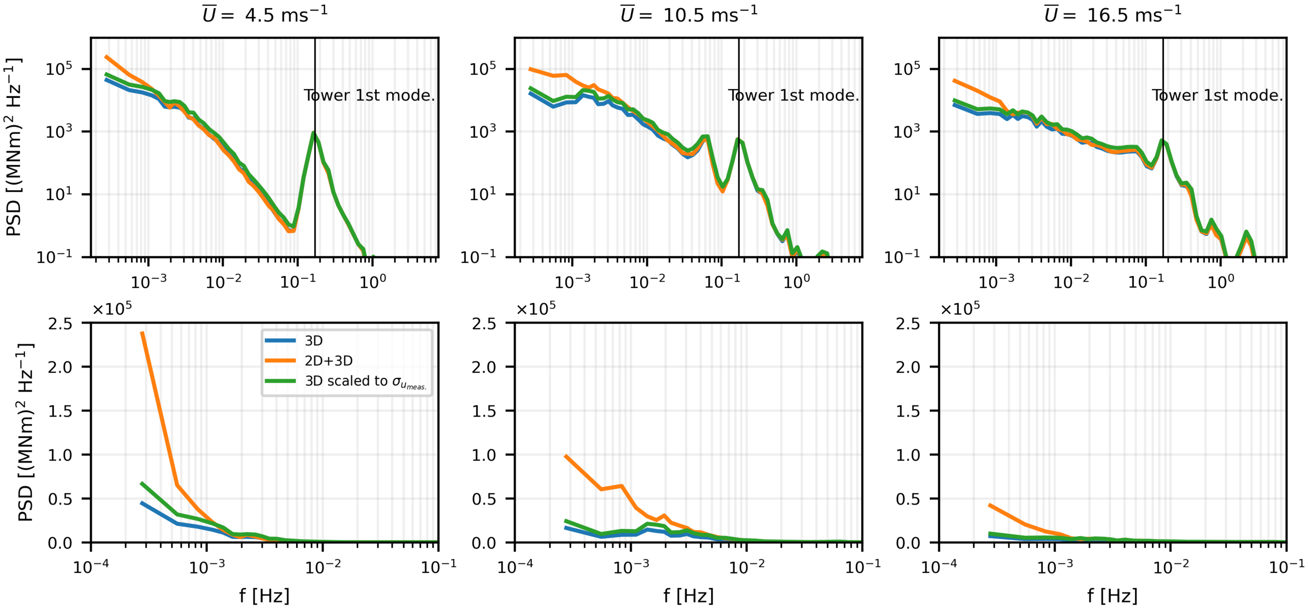

Figure 15. PSD of tower base fore-aft moment in response to 3D, 2D+3D, and scaled 3D turbulent wind fields (Monopile configuration). The top row shows the full frequency range, including the high-frequency response on a log-log plot. The straight vertical line at $f = 0.17$ Hz intersects with the tower's first mode peak. The bottom row zooms into the low-frequency response on a semi-log plot

as input, incorporating uniform background free-stream conditions with and without large-scale fluctuations for comparative analysis. The wake deficit model corresponds to the Ainslie eddy viscosity model, and we apply a spectral filter to the incoming wind field to isolate scales larger than one rotor diameter, which drives wake dynamics. Fig. 18 shows the wind farm layout and two snapshots from the flow simulations, where the input wind fields contain 3D and 2D+3D turbulence, respectively. The flow in both cases behaves distinctly, as the wake flow exhibits significantly more meandering in the presence of large-scale horizontal coherent structures.

One-hour flow simulations were used to evaluate the Damage Equivalent Loads (DELs) for wind turbine components. Figures 19 and 20 illustrate the effect of large-scale structures on wind turbine tower and blade loads, respectively. Stochastic uncertainty is reduced by running six wind farm simulations for each wind speed based on different seed values used as input to generate turbulent wind fields. Results show that wind turbines outside the wake flow experience similar loads, irrespective of the input wind field. However, wind turbines inside the wake flow experience large tower-base and blade-root loads in the presence of 2D turbulence or large-scale coherent structures. One reason could be that wind turbines inside the wake often experience partial wakes, where the wake flow covers only a part of the rotor; hence, the blades experience a significant increase in fatigue loading. Due to the large-scale structures, higher wake meandering is present within the wind farm, which increases the likelihood of a wind turbine being affected by a partial wake flow.

https://doi.org/10.5194/wes-2025-286
Preprint. Discussion started: 22 January 2026

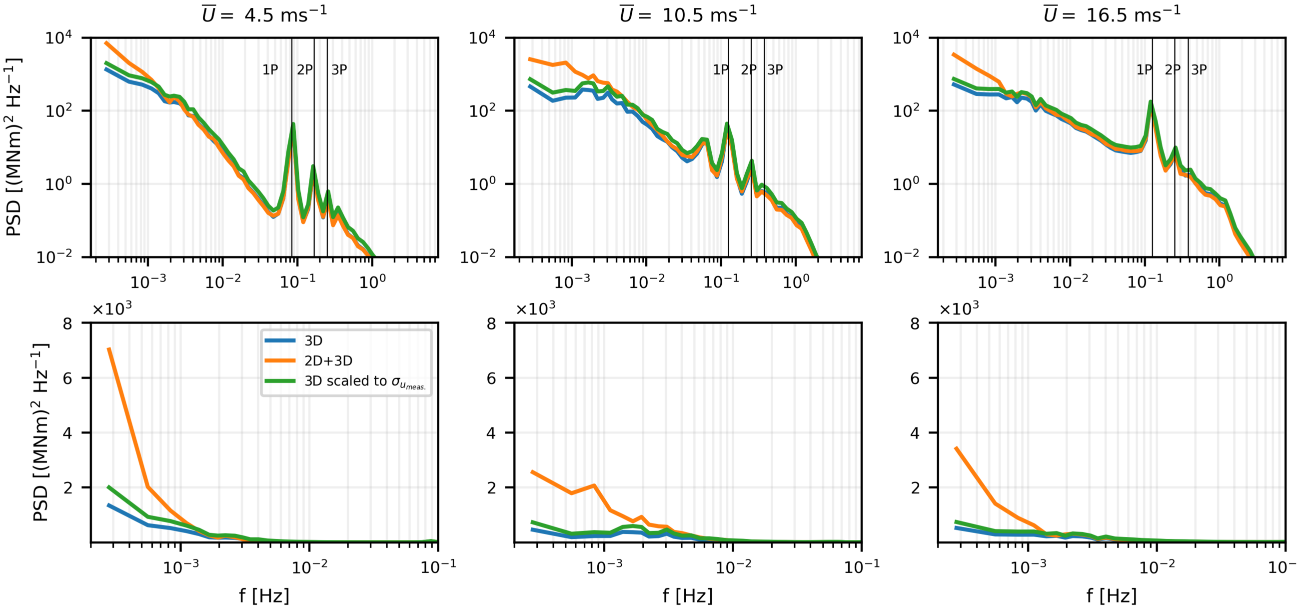

Figure 16. PSD of blade root flapwise moment in response to 3D, 2D+3D, and scaled 3D turbulent wind fields (Monopile configuration). The top row shows the full frequency range, including the high-frequency response on a log-log plot. The straight vertical lines intersect with the 1P, 2P, and 3P frequencies of the turbine rotor. The bottom row zooms into the low-frequency response on a semi-log plot

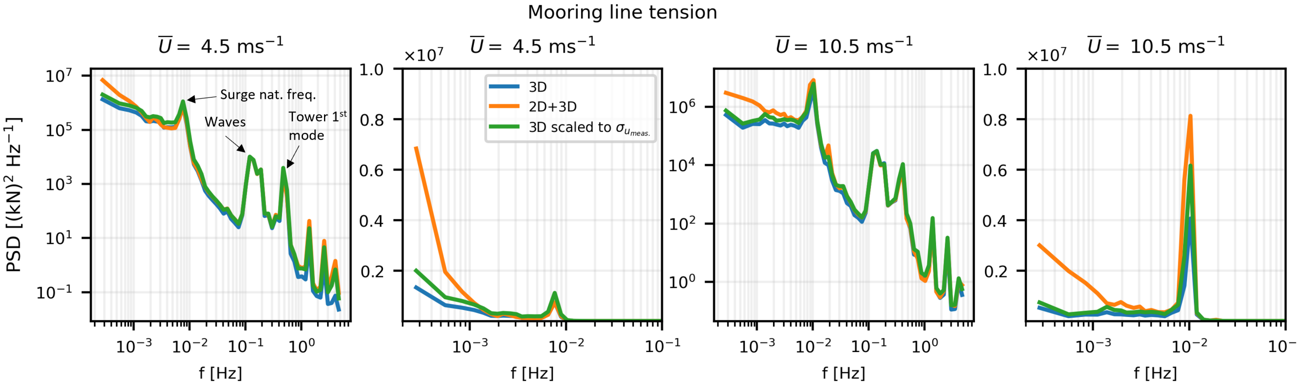

Figure 17. The response of the mooring line tension to different wind fields. These responses are shown for two wind speeds, i.e., 4.5 and 10.5 ms^{-1}. The first and third columns represent the full frequency range on a log-log plot, while the second and fourth columns zoom into the low frequencies. Peaks corresponding to surge, waves, and tower motion are also indicated

The effect of large-scale coherent structures on wind farm power production is also investigated. Fig. 21 shows the mean capacity factor estimation of all wind turbines inside the wind farm at the mean wind speed of 10 ms^{-1}. While the wind

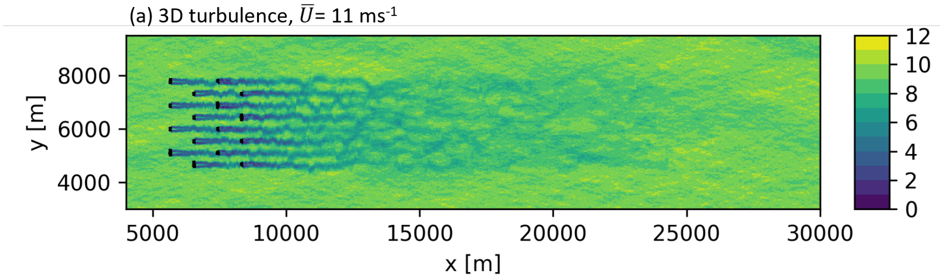

(a) 3D turbulence, $\bar{U}$= 11 ms^{-1}

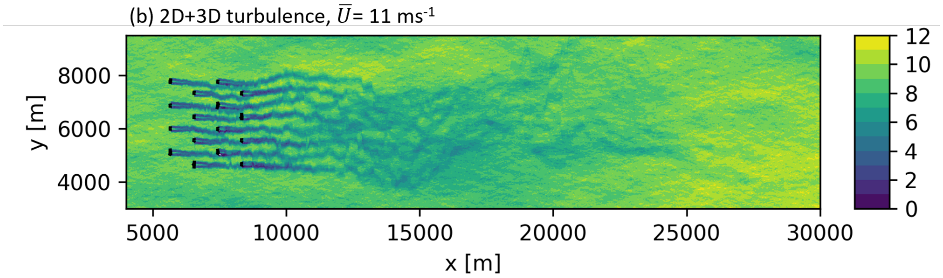

(b) 2D+3D turbulence, $\bar{U}$= 11 ms^{-1}

Figure 18. Two snapshots of the wind farm flow simulation containing (a) 3D turbulence, and (b) 2D+3D turbulence. The colorbar on the left represents the wind speed gradient. Mean wind speed during this specific simulation was 11 ms^{-1}

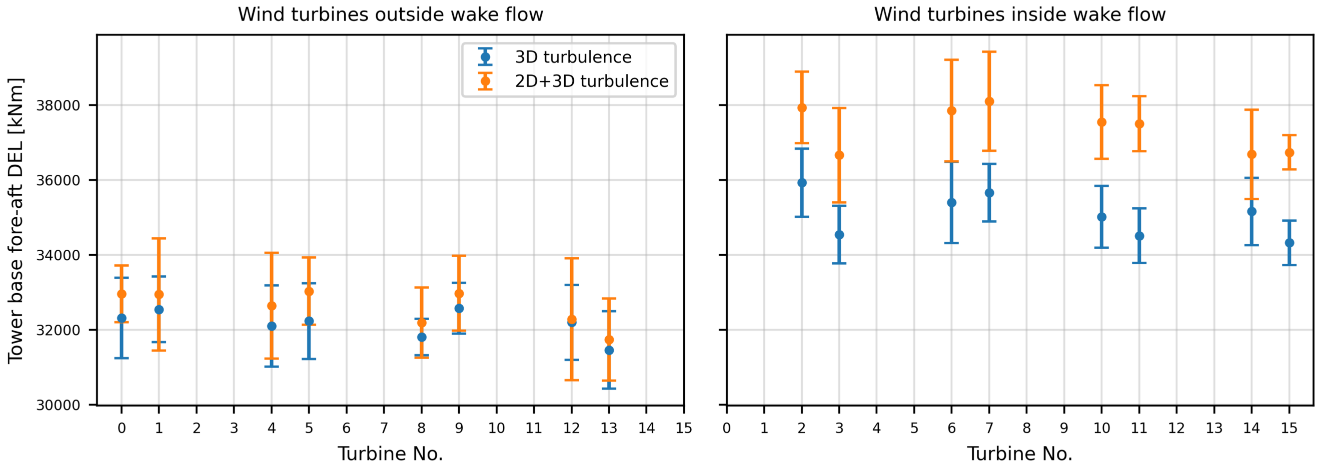

Figure 19. Mean tower base fore-aft Damage Equivalent Loads (DELs) for wind turbines in the first two rows (left), and for wind turbines inside the wake flow in the last two rows (right) at $U = 10$ ms^{-1}. Error bars represent ±1 standard deviation.

turbines outside the wake flow are expected to have similar capacity factors, the wind turbines inside the wake flow behave very differently in the presence of 2D turbulence. Large-scale wake meandering leads to an increase in wind speed observed

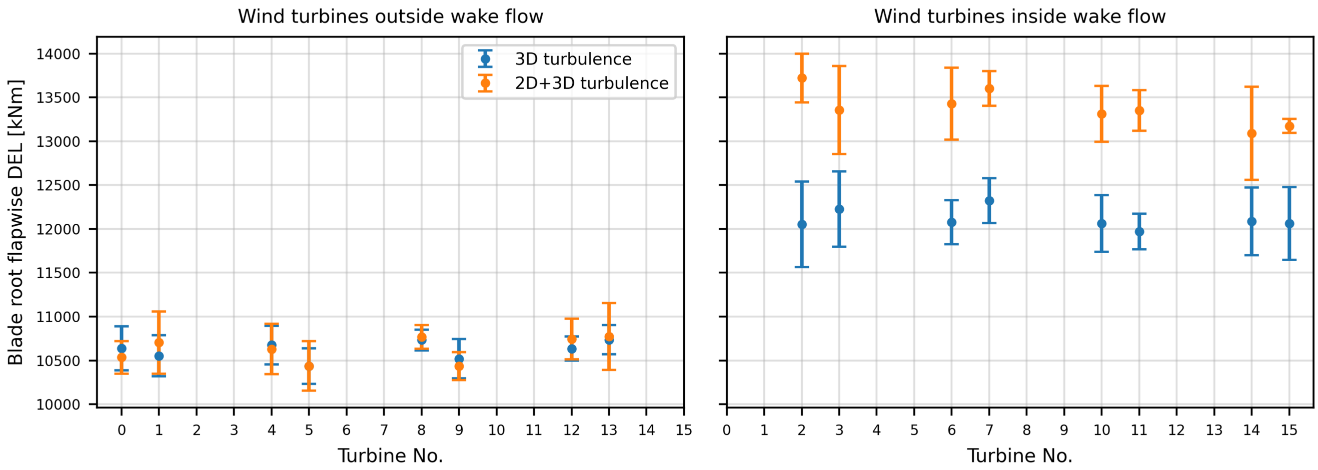

Figure 20. Mean blade root flapwise Damage Equivalent Loads (DELs) for wind turbines in the first two rows (left), and for wind turbines inside the wake flow in the last two rows (right) at $U = 10\ \mathrm{ms}^{-1}$. Error bars represent ±1 standard deviation.

by the wind turbines; hence, an increase in power output. However, as shown earlier, this power increase comes at the expense of increased blade and tower loads.

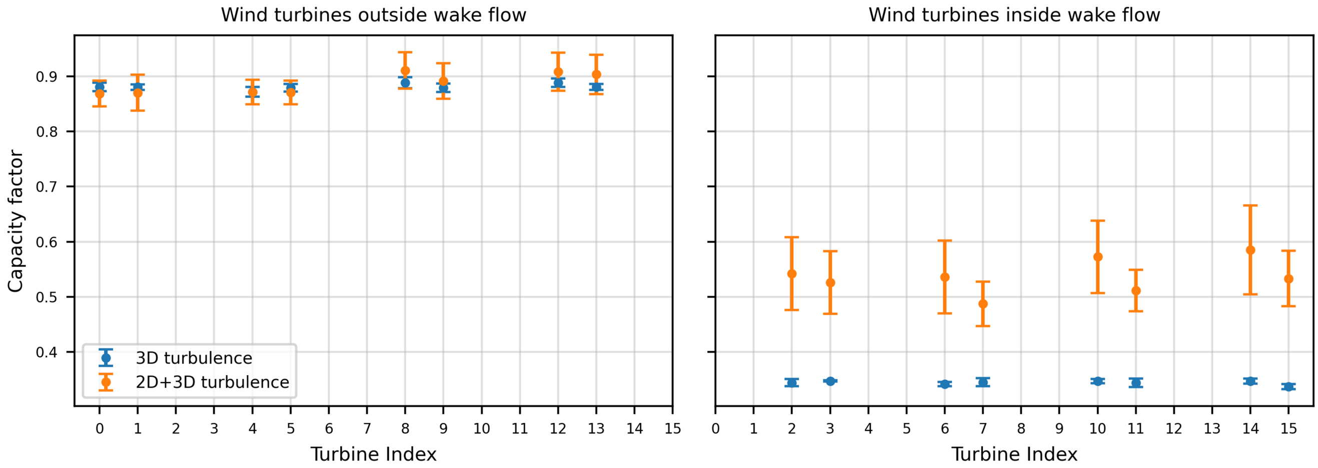

Figure 21. Mean capacity factor for wind turbines in the first two rows (left), and for wind turbines inside the wake flow in the last two rows (right) at $U = 10\ \mathrm{ms}^{-1}$. Error bars represent ±1 standard deviation.

4 Discussion

The wind statistics shown in figure 6 illustrates the BLH distributions where site B and C have a lower BLH. The results in figure 9 show that the impact of boundary layer height, here used as a proxy for the atmospheric state, has a significant impact on farm efficiency considering a large 100 turbine farm with 15 MW IEA turbines. The results show that when considering the wind statistics at site A, B, and C in combination with the numerical study of farm efficiency, the overall estimated annual farm efficiency of the sites varies between 0.61 and 0.65 where it is 0.61 for site A, 0.62 for B, and 0.64 for site C. It is here important to point out that these numbers do not include wind direction distributions since the number of high fidelity simulations for such an investigation was not possible within this study. Therefore, this study considers the BLH distribution assuming one wind direction. The variation in impact under these assumptions is clear. Considering the staggered farm layout, its size, and assuming a reasonable large share of a dominant wind direction, the influence on the impact variation is assumed to be low. Therefore, these values should not be considered to represent realistic annual efficiency for these sites. However, these results can be used to validate engineering models, where a complete assessment of the wind direction is also feasible to include.

The evaluation of the uncertainty of the applied method shows that the uncertainty for site B is ± 0.04 resulting in an efficiency between 0.54 and 0.62, implying that the results at site B have a small overestimation. Knowing the uncertainty at site B, where the quality of the WRF simulation is expected to be lowest (compared to site A and C) due to its proximity to land (Floors et al., 2018; Hahmann et al., 2020) we assume the uncertainty to be highest at site B. Therefore, considering the conditions at site B to be representative, we assume that the uncertainty at site A and C is within ± 0.04.

Taking into account the variation between sites A, B, and C, which have different atmospheric characteristics. The result shows a variation in impact, where site C has a generally lower BLH and also the lowest farm efficiency. Taking into account seasonal variations, i.e., the spring and summer periods at site C, it is further shown that the BLH has an impact on farm efficiency. It is a well known fact that sites in the Baltic Sea, i.e., site C, do experience a large extent of low BLH and low level jets during the spring and summer period (Hallgren et al., 2023) and that is also here reflected in the results.

The results show that the impact of 2D coherent structures, and their large scale-scale turbulence structures, impact the wind turbine loads and in some cases decreases and other cases increases the dynamic response. For a solitary fixed-bottom offshore wind turbine, Syed et al. (2024) finds that when high-frequency turbulence spectra are matched, but realistic low-frequency fluctuations are added to the simulation, the damage equivalent loads increase slightly, especially for the tower base fore-aft loads, which increase $\approx 4\%$. However, if one matches the measured turbulence level, but redistributes the spectral energy more realistically to include the low-frequency variations, i.e. moving energy from the high frequencies to the low frequencies, then the loads generally decrease, in some cases more than 10%. In this contribution, where we consider a whole wind farm, the impact of low-frequency fluctuations is larger for the turbines inside the wind farm. For some wind directions, low-frequency fluctuations of the transverse component of the wind field cause stronger meandering of the wakes. This, in turn, increases tower base fore-aft and blade root flapwise damage equivalent loads with up to 15%. The IEC standard (IEC, 2005) does not contain these low-frequency variation, probably because it is mainly based on on-shore measurements of turbulence where the normal 3D turbulence dominates the 2D turbulence.

In particular, this impacts the equivalent damage loads when considering wind turbines inside wake flows. Again, it should be pointed out that these simulations only concern one wind direction, so it is difficult to generalize. The parameters of the Syed and Mann (2024a) model vary, in general, very similarly at the different sites, if they are viewed as functions of wind speed and stability. Comparing figures 2 from site d (Høvsøre) and 4 from site e (FINO1), the 2D-turbulence intensity c and 2D anisotropy parameter ψ change consistently with wind speed and stability. Especially at larger wind speeds the c parameter is larger for unstable stratification. Site e is more 2D-isotropic at low-frequencies than site d, but the difference is not great. Unfortunately, we do not have similar turbulence measurements in the Baltic, so comparison between the two seas is difficult. We do know that the atmosphere above the North Sea is more unstable and with higher BLH, so, according to our investigations, the strength if the 2D low-frequency variation should be stronger and the dynamic loads attributable to wake meandering might be higher in the North Sea. However, under unstable conditions, the wake disperse more rapidly possibly reducing the dynamic loads in waked situations. More investigations are needed on a final verdict on dynamic load variations in the different seas.

5 Conclusions

This study demonstrates that atmospheric boundary layer height (BLH) is a critical factor influencing wind farm performance and turbine loads. Sites with lower BLH, such as those in the Baltic Sea, exhibit reduced farm efficiency compared to North Sea locations, highlighting the importance of regional climatology in planning and modeling large offshore wind farms. While efficiency estimates ranged between 0.61 and 0.65 for the sites studied, these values are based on simplified assumptions and should primarily serve as validation benchmarks for engineering models. Uncertainty analysis indicates that BLH retrievals from mesoscale models can deviate significantly from lidar observations, introducing potential biases in efficiency predictions. This underscores the need for improved BLH representation in atmospheric models. The impact of large-scale, low-frequency turbulence structures on turbine loads is substantial, particularly within wind farms where wake meandering amplifies fatigue loading. Current design standards, which neglect these low-frequency variations, may underestimate structural demands. Future work should incorporate directional variability, expand load assessments across diverse atmospheric regimes, and refine turbulence modeling to ensure reliable performance for next-generation offshore wind farms.

Code and data availability. The model implementation code and the simulation data files for different cases resulting from the parametric study can be provided upon request.

Appendix A: Seasonal variation in boundary layer height and wind speed

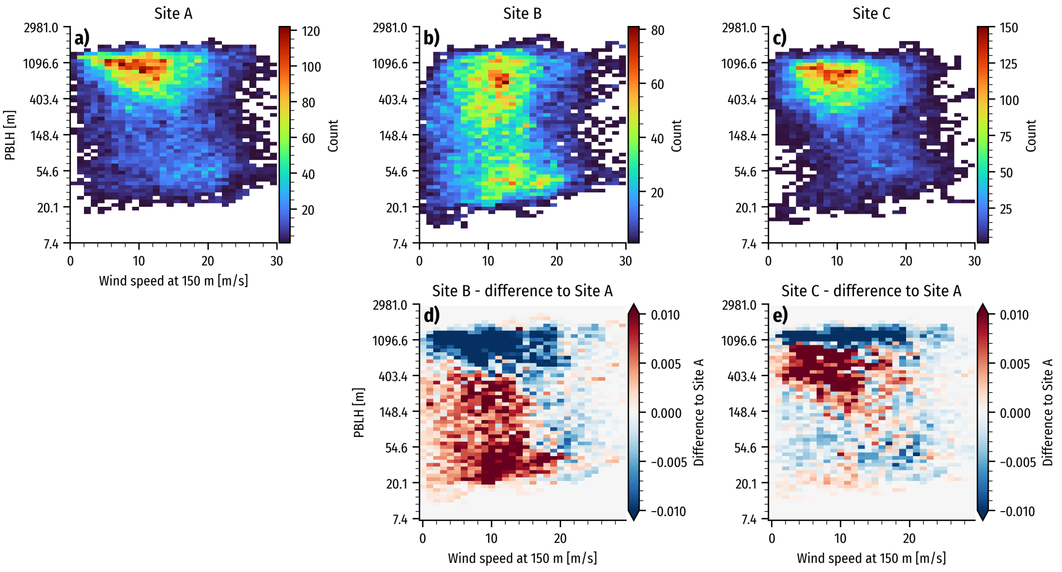

Figure A1. Winter (DJF)

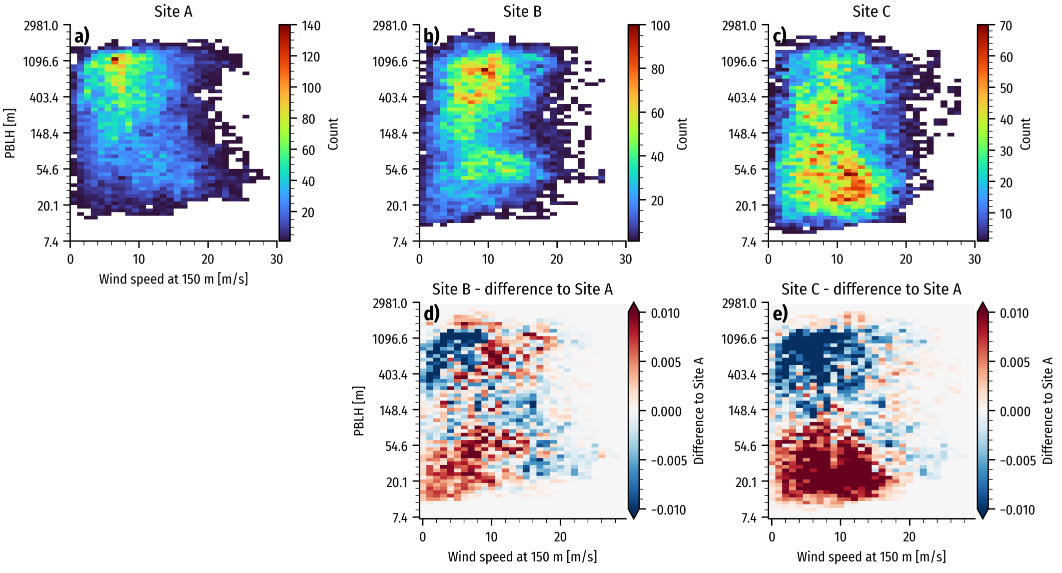

Figure A2. Spring (MAM)

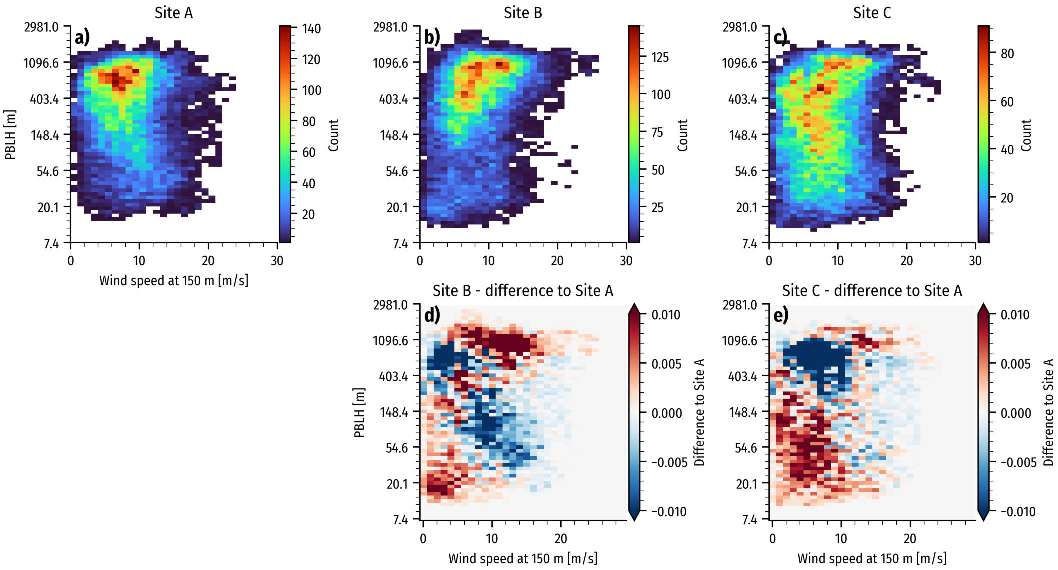

Figure A3. Summer (JJA)

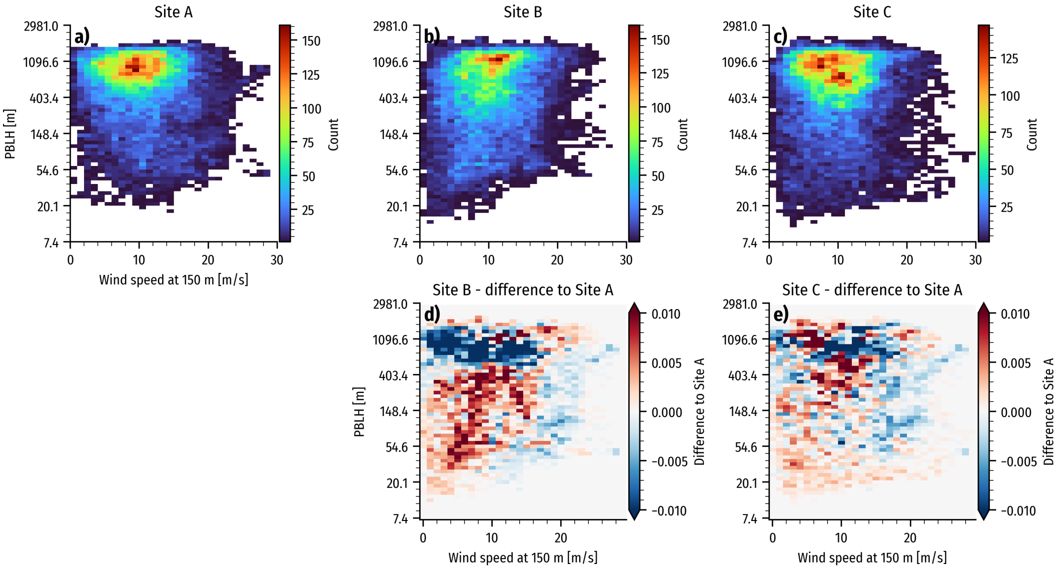

Figure A4. Autumn (SON)

Author contributions. SI coordinated the development of the article. The scope and focus of the study where developed by SI, JG, WC, BO, AM, MS and JM. BO performed the WRF simulations and the climatology assessment. AM performed the CFD simulations. CMB performed the uncertainty evaluation. AHS performed the load assessment. The manuscript was written by all authors.

385 *Competing interests.* Two of the (co-)authors are a members of the editorial board of Wind Energy Science.

Acknowledgements. This work has been funded by the FLOW project (Atmospheric Flow, Load and pOwer for Wind energy) within the EU Horizon Europe programme (grant no. 101084205). Part of this research was conducted by participation of the Marie Sklodowska-Curie Actions (grand no. 101119550), the AptWind project.

References

Allaerts, D. and Meyers, J.: Gravity waves and wind-farm efficiency in neutral and stable conditions, Boundary-layer meteorology, 166, 269–299, 2018.

Angelou, N., Mann, J., and Dubreuil-Boisclair, C.: Revealing inflow and wake conditions of a 6 MW floating turbine, Wind Energy Science, 8, 1511–1531, https://doi.org/10.5194/wes-8-1511-2023, 2023.

Archambeau, F., Méchitoua, N., and Sakiz, M.: Code Saturne: A finite volume code for the computation of turbulent incompressible flows-Industrial applications, International Journal on Finite Volumes, 1, http–www, 2004.

Floors, R., Hahmann, A. N., and Peña, A.: Evaluating mesoscale simulations of the coastal flow using lidar measurements, Journal of Geophysical Research: Atmospheres, 123, 2718–2736, 2018.

Gaertner, E., Rinker, J., Sethuraman, L., Zahle, F., Anderson, B., Barter, G., Abbas, N., Meng, F., Bortolotti, P., Skrzypinski, W., Scott, G., Feil, R., Bredmose, H., Dykes, K., Sheilds, M., Allen, C., and Viselli, A.: Definition of the IEA 15-Megawatt Offshore Reference Wind Turbine, Tech. rep., International Energy Agency, https://www.nrel.gov/docs/fy20osti/75698.pdf, 2020.

Guo, J., Zhang, J., Shao, J., Chen, T., Bai, K., Sun, Y., Li, N., Wu, J., Li, R., Li, J., Guo, Q., Cohen, J. B., Zhai, P., Xu, X., and Hu, F.: A merged continental planetary boundary layer height dataset based on high-resolution radiosonde measurements, ERA5 reanalysis, and GLDAS, Earth System Science Data, 16, 1–14, https://doi.org/10.5194/essd-16-1-2024, 2024.

Hahmann, A. N., SÄ«le, T., Witha, B., Davis, N. N., Dörenkämper, M., Ezber, Y., García-Bustamante, E., González-Rouco, J. F., Navarro, J., Olsen, B. T., and Söderberg, S.: The making of the New European Wind Atlas – Part 1: Model sensitivity, Geoscientific Model Development, 13, 5053–5078, https://doi.org/10.5194/gmd-13-5053-2020, 2020.

Hallgren, C., Aird, J. A., Ivanell, S., Körnich, H., Vakkari, V., Barthelmie, R. J., Pryor, S. C., and Sahlée, E.: Machine learning methods to improve spatial predictions of coastal wind speed profiles and low-level jets using single-level ERA5 data, Wind Energy Science Discussions, 2023, 1–30, 2023.

Hu, X.-M., Nielsen-Gammon, J. W., and Zhang, F.: Evaluation of Three Planetary Boundary Layer Schemes in the WRF Model, Journal of Applied Meteorology and Climatology, 49, 1831 – 1844, https://doi.org/10.1175/2010JAMC2432.1, 2010.

IEC: IEC 61400-1. Wind turbines – design requirements, International Electrotechnical Commission, 3 edn., 2005.

Ivanell, S., Chanprasert, W., Lanzilao, L., Bleeg, J., Meyers, J., Mathieu, A., Juhl Andersen, S., Mouradi, R.-S., Dupont, E., Olivares-Espinosa, H., et al.: An inter-comparison study on the impact of atmospheric boundary layer height on gigawatt-scale wind plant performance, Wind Energy Science Discussions, 2025, 1–34, 2025.

Jiménez, P. A., Dudhia, J., González-Rouco, J. F., Navarro, J., Montávez, J. P., and García-Bustamante, E.: A Revised Scheme for the WRF Surface Layer Formulation, Monthly Weather Review, 140, 898 – 918, https://doi.org/10.1175/MWR-D-11-00056.1, 2012.

Larsen, G. C., Madsen, H. A., Thomsen, K., and Larsen, T. J.: Wake meandering: a pragmatic approach, Wind Energy: An International Journal for Progress and Applications in Wind Power Conversion Technology, 11, 377–395, 2008.

Liew, J., Göçmen, T., Lio, A. W. H., and Larsen, G. C.: Extending the dynamic wake meandering model in HAWC2Farm: a comparison with field measurements at the Lillgrund wind farm, Wind Energy Science, 8, 1387–1402, 2023.

Mann, J.: The spatial structure of neutral atmospheric surface-layer turbulence, J. Fluid Mech., 273, 141–168, 1994.

Mann, J.: Wind field simulation, Probabilistic engineering mechanics, 13, 269–282, 1998.

Mann, J., Patel, A., Sjoholm, M., Thorsen, G., Simon, E., Hung, L., and Gottschall, J.: An experimental campaign to measure turbulence in the marine boundary layer, under preparation, 2026.

Meng, F., Lio, W. H., and Barlas, T.: DTUWEC: an open-source DTU Wind Energy Controller with advanced industrial features, Journal of Physics: Conference Series, 1618, 022 009, 2020.

Mulet-Benzo, C., Black, A., and Gottschall, J.: Comparing atmospheric boundary layer heights from vertical profiling scanning lidars to ERA5 and WRF, Wind Energy Science Discussions, 2025, 1–30, https://doi.org/10.5194/wes-2025-155, 2025.

Olsen, B. T. E., Hahmann, A. N., Alonso-de Linaje, N. G., Žagar, M., and Dörenkämper, M.: Low-level jets in the North and Baltic seas: mesoscale model sensitivity and climatology using WRF V4.2.1, Geoscientific Model Development, 18, 4499–4533, https://doi.org/10.5194/gmd-18-4499-2025, 2025.

Olson, J. B., Kenyon, J. S., Angevine, W. A., Brown, J. M., Pagowski, M., and Sušelj, K.: A Description of the MYNN-EDMF Scheme and the Coupling to Other Components in WRF–ARW, https://doi.org/10.25923/N9WM-BE49, publisher: Earth System Research Laboratory (U.S.), Global Systems Division, 2019.

Syed, A. H. and Mann, J.: A model for low-frequency, anisotropic wind fluctuations and coherences in the marine atmosphere, Boundary-Layer Meteorology, 190, 1, 2024a.

Syed, A. H. and Mann, J.: Simulating low-frequency wind fluctuations, Wind Energy Science, 9, 1381–1391, https://doi.org/10.5194/wes-9-1381-2024, 2024b.

Syed, A. H., Hannesdóttir, Á., and Mann, J.: Impact of low-frequency fluctuations on loads of a fixed-bottom offshore reference wind turbine, in: Journal of Physics: Conference Series, vol. 2767, p. 052041, IOP Publishing, 2024.

Veers, P., Dykes, K., Lantz, E., Barth, S., Bottasso, C. L., Carlson, O., Clifton, A., Green, J., Green, P., Holttinen, H., Laird, D., Lehtomäki, V., Lundquist, J. K., Manwell, J., Marquis, M., Meneveau, C., Moriarty, P., Munduate, X., Muskulus, M., Naughton, J., Pao, L., Paquette, J., Peinke, J., Robertson, A., Rodrigo, J. S., Sempreviva, A. M., Smith, J. C., Tuohy, A., and Wiser, R.: Grand challenges in the science of wind energy, Science, 366, eaau2027, https://doi.org/10.1126/science.aau2027, 2019.

Xi, X., Yang, Q., Liu, C., Shupe, M. D., Han, B., Peng, S., Zhou, S., and Chen, D.: Evaluation of the Planetary Boundary Layer Height From ERA5 Reanalysis With MOSAiC Observations Over the Arctic Ocean, Journal of Geophysical Research: Atmospheres, 129, e2024JD040 779, https://doi.org/10.1029/2024JD040779, 2024.

Zhang, X., Bao, J.-W., Chen, B., and Grell, E. D.: A Three-Dimensional Scale-Adaptive Turbulent Kinetic Energy Scheme in the WRF-ARW Model, Monthly Weather Review, 146, 2023 – 2045, https://doi.org/10.1175/MWR-D-17-0356.1, 2018.